Triangulating the height of cosmic noise absorption: A method for estimating the characteristic energy of precipitating electrons

P. Wild,[1] F. Honary,[1] A. J. Kavanagh,[1] and A. Senior[1]

Received 2 June 2010; revised 6 September 2010; accepted 9 September 2010; published 21 December 2010.

[1] Energetic electrons (tens to hundreds of keV) deposit significant energy into the D layer of the ionosphere. Riometers provide a means of monitoring this electron precipitation by measuring the associated cosmic noise absorption (CNA), but individually they are incapable of resolving the associated energy. However, the combination of two imaging riometers with overlapping beams allows an estimate of the height of peak CNA and so the associated energy to be made. We examine two methods for estimating the height of CNA using data from two imaging riometers in northern Fennoscandia; a 3-D reconstruction of CNA using Occam's inversion and a technique based upon the triangulation of discrete absorption structures are developed. We compare these two methods with the results from a previously published technique. It is found that for the case studies and test phantoms the height triangulation and 3-D reconstruction offer improvement over previous methods. These techniques are tested by comparison with data from the EISCAT incoherent scatter radar. Observations show good correlation between the estimates of peak height of CNA from EISCAT and from the triangulation and 3-D reconstruction methods for this case. Three case studies are examined in detail, a slowly varying absorption, afternoon spike, and evening absorption spike event. Estimates of the characteristic energy are made. The substorm event had a characteristic energy of ~5 keV, whereas the characteristic energy for the morning event was 17–20 keV. Analyses indicate the afternoon spike event having characteristic energy greater than 100 keV.

Citation: Wild, P., F. Honary, A. J. Kavanagh, and A. Senior (2010), Triangulating the height of cosmic noise absorption: A method for estimating the characteristic energy of precipitating electrons, *J. Geophys. Res.*, *115*, A12326, doi:10.1029/2010JA015766.

1. Introduction

[2] The precipitation of electrons into the atmosphere is an important step in the transfer of energy and momentum through the coupled solar-terrestrial environment. Electrons with energies from 10s to 100s of keV penetrate to mesospheric heights (60–100 km) enhancing the ionized D layer of the atmosphere and affecting the resultant ion chemistry [*Rees*, 1989]. These electrons are injected from the magnetotail during substorms [*Arnoldy and Chan*, 1969] and undergo gradient-curvature drift into the dayside ionosphere; along the drift path they interact with whistler mode chorus waves which scatter a fraction of the electron population into the bounce loss cone, resulting in a diurnal variation of precipitation maximizing in the morning sector [e.g., *Kavanagh et al.*, 2004]. Direct measurement of this scattering process and loss cone electrons are difficult to obtain on a regular basis; however ground-based instruments can provide a proxy for the occurrence of electron precipitation. By monitoring the absorption of cosmic radio noise along a fixed beam path, riometers [*Little and Leinbach*, 1959] provide an indication of the increased electron density in the D layer and consequently the associated electron precipitation. The continuous monitoring by riometers is a valuable resource but its utility is vastly enhanced when used in conjunction with other instruments [e.g., *Kavanagh et al.*, 2007; *Collis and Hargreaves*, 1997]. The major disadvantage of riometer estimates of precipitation is the lack of information on the altitude distribution of the cosmic noise absorption (CNA); knowing the height of peak CNA can lead to an estimate of the characteristic energy of the precipitating electrons. *Terkildsen et al.* [2004] provided a means of height estimation through the use of a vertical parallax technique; this method, though successful, is limited as it requires the CNA event to have a east-west motion and it assumes a constant altitude over the course of the event.

[3] In this paper we use two closely located riometers with overlapping fields of view to determine a new method of estimating the height of peak CNA. We apply tomographic reconstruction to the absorption problem and also develop a method using height triangulation. These methods are evaluated using test data and compared with the method of *Terkildsen et al.* [2004]. A case where incoherent scatter radar data were available is shown; this provides an independent check on the two techniques.

[1]Department of Physics, Lancaster University, Lancaster, UK.

0148-0227/10/2010JA015766

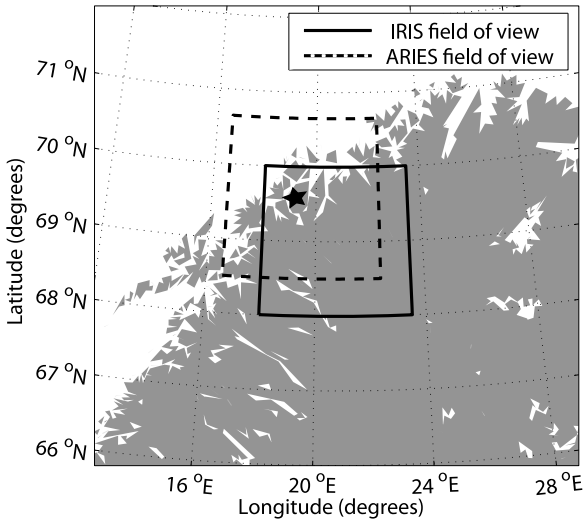

Figure 1. Plot showing the overlapping fields of view of ARIES and IRIS at 90 km altitude. Star, location of EISCAT mainland radar.

[4] *Stauning* [1996] describes various absorption processes which can be observed by a riometer. The location of the riometer dictates which type of absorption phenomena are seen. IRIS at Kilpisjärvi and ARIES are located at auroral altitudes. We apply the techniques to three separate case studies employing data from October to December 2007; these events show differing characteristics and are categorized by *Stauning* [1996] as (1) a slowly varying absorption event, (2) a substorm, and (3) an afternoon absorption spike. The characteristic energy of the precipitating electrons based on the height estimate is calculated for each event.

2. Instrumentation

[5] Observations of the CNA events have been provided by the Advanced Rio-Imaging Experiment in Scandinavia (ARIES) and the Imaging Riometer for Ionospheric Studies (IRIS) at Kilpisjärvi. These two riometers have been chosen because of their overlapping fields of view, as seen in Figure 1.

[6] IRIS is located in Kilpisjärvi (69.05°N, 20.79°E); it comprises of 64 cross dipole antennas, arranged in a square, on north-south lines. The output from these antennas are fed into a phasing network based on a Butler matrix. The output creates a system with 49 beams, with beam widths varying between 13° and 16° for center and edge beams, respectively [*Browne et al.*, 1995]. Projected to a height of 90 km, this translates to a 250 × 250 km field of view.

[7] ARIES (located in Norway at 69.63°N, 19.52°E) employs a Mills cross system, compared to IRIS's filled array. This is a set of two perpendicular arms of 32 cross dipole antennas [*Honary et al.*, 2005]. Beam forming is a two stage process; the two arms of the cross effectively create 32 fan beams in the north-south direction and 32 fan beams in the East-West direction. Cross correlation of the fan beams creates 1024 combinations of which there are 556 useful pencil beams [*Grill*, 2007]. The sidelobe power for these beams ranges from −17 dB (center) to −13 dB (edge) with an average of −15 dB relative to the main lobe, which is comparable to the values quoted for the IRIS system by *Detrick and Rosenberg* [1990]. The central ARIES beams have a width of ~6°, much smaller compared with the ~13° central IRIS beam. Initial site surveys found no man-made interference in the ARIES observing frequency band and on-site equipment were shielded to minimize corruption of the data. Data used in this manuscript are free from man-made interference. Quiet day curves for ARIES data for this paper were created by taking known quiet days and fitting a Fourier series to the log of raw power, along with fit to the log of the calibration power. Radio stars within narrow riometer beams can lead to scintillation in the data; however modeling of the ARIES (and IRIS) radiation patterns together with knowledge of the stars position in the sky allows us to ignore data from beams contaminated with scintillation [*Grill*, 2007].

[8] Measurements obtained from the colocated incoherent scatter radar, EISCAT [*Rishbeth and van Eyken*, 1993] marked as a star in Figure 1 are also utilized as a validity check on the techniques for height determination.

3. Methods

3.1. Height Triangulation

[9] Using the recorded absorption in the beams of the two riometers, a spatial image of the absorption can be produced for both ARIES and IRIS. The pointing direction of each beam is used to calculate the location at heights between 70 and 150 km. At each height the values of absorption are interpolated onto a 2-D grid. Linear interpolation is used to populate the gaps between the beam centers and create the absorption image. This is achieved using the Multi-instrument Analysis Toolkit (MIA) [*Marple and Honary*, 2004]. An assumption is made that the recorded power is located at the beam center. In the case of IRIS the corner beams have ill-defined main lobes and significant sidelobes and thus not used in the creation of the images, and with ARIES the central 556 beams are used.

[10] Setting a spatial grid on which the absorption values of both riometers are calculated, direct comparison of the two images can be made. A spatial grid between 66.5°N–71.5°N (with 0.05° increments) and 13.5°E–26.5°E (with 0.10° increments) is used. By projecting the images to heights between 70 and 150 km, with a 2 km increment, the linear cross correlation of the two images at each height can be calculated. The height of best correlation corresponds to the best estimate of the peak height of CNA. Only results that have a correlation greater than 0.6 will be considered for this study. This cutoff value is a heuristic choice, giving a trade off between number of resolved events and confidence value of the result. A resolution of 10 s is used for the absorption values taken from IRIS and ARIES, unless otherwise stated. The standard deviation associated with the height estimation is generated by uncertainties in the cross correlation. These uncertainties encompass such things as height ambiguity, vertical extent of the peak, etc. This is expressed as the standard deviation in the cross correlation for each altitude. The standard deviation in the height triangulation is obtained in the same manner as in the work of *Ashrafi and Kosch* [2004]. For each cross correlation value, a new cross correlation value is created that falls within the normal distribution of the original value. A second-order polynomial curve is fitted to the new values. The curves maximum value is the peak height of CNA.

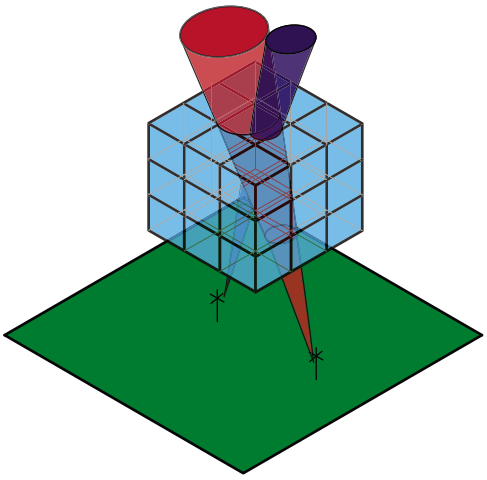

Figure 2. Tomographic problem for CNA. Voxels are discretized between 69° and 70.4° in latitude, 18.5°–22.7° in longitude, and 55–120 km in altitude. They are spaced 0.2°, 0.64°, and 5 km, respectively. For this volume element 18 IRIS beams (example beam shown in red) and 306 ARIES beams (example beam shown in purple) are used.

Repeating this process numerous times allows measurement of the uncertainty on the peak height of CNA.

3.2. Tomography

[11] The second method employed is to create a 3-D reconstruction of the absorption using tomographic methods. Tomography is the process of recreating the internal structure of an object using intensity data from the integral along the line of sight through the object [*Gustavsson*, 2000]. Recently tomographic methods have been applied to emission processes in the upper atmosphere. Data from measurements of total electron content (TEC) between satellites and ground receivers to create 2-D maps of electron density in the ionosphere have been widely investigated [*Fougere*, 1995; *Bhuyan et al.*, 2002]. Related work reconstructing the optical emissions in the ionosphere using ground based cameras have been implemented by *Gustavsson* [2000] and *Semeter and Mendillo* [1997]. Tomography is implemented in this study to reconstruct the 3-D structure of CNA in the D region ionosphere using 2-D absorption images recorded by imaging riometers. Figure 2 illustrates the geometry of the problem.

[12] The absorption volume is discretized into small volume elements called "voxels". With a volume constructed with a relatively conservative number of voxels (7 × 7 × 13) the problem still has more degrees of freedom than is supported by the data (637 voxels compared to 324 beams). This leads to what is known as an "ill posed" problem. Ill-posed problems suffer from having numerous solutions, where only a portion are feasible solutions. Thus the problem needs to be regularized to eradicate the unfeasible solutions (sections 3.2.2).

3.2.1. Forward Model

[13] With any tomographic procedure detailed knowledge of the forward model is required. The amplitude of a wave along the line of sight l varies by

$$A = A_0 \exp \int_0^l -\kappa \mathrm{d}l. \tag{1}$$

A_0 is the peak amplitude. κ is the absorption coefficient (nepers/meter). The intensity of a wave is proportional to the amplitude squared,

$$I = \left(A_0 \exp \int_0^l -\kappa \mathrm{d}l \right)^2. \tag{2}$$

In the absence of absorption $\kappa = 0$ and $I_0 = A_0^2$. Therefore the intensity becomes

$$I = I_0 \exp \int_0^l -2\kappa \mathrm{d}l. \tag{3}$$

The cosmic noise absorption measured by a riometer is a measure of the noise power, P compared to the quiet noise power P_Q, the power if there was no absorption. Absorption measured by a riometer in decibels is Absorption = $-10\log_{10}(P/P_Q)$. The received RF power in a given direction is proportional to the square of the directivity (the gain) [*Detrick and Rosenberg*, 1990] multiplied by the sky noise intensity. Thus the total power received by the riometer is then the integral of the intensity of the wave in all solid angles (Ω), weighted by the gain,

$$P = c \int_\Omega G(\Omega) I_0(\Omega) \exp \int_0^l -2\kappa(l,\Omega) \mathrm{d}l \mathrm{d}\Omega, \tag{4}$$

where c is a constant of proportionality. Thus the absorption in a riometer becomes, noting power on a quiet day means $\kappa = 0$.

$$\text{Absorption} = -10 \log_{10} \left(\frac{c \int_\Omega G(\Omega) I_0(\Omega) \exp \int_0^l -2\kappa(l,\Omega) \mathrm{d}l \mathrm{d}\Omega}{c \int_\Omega G(\Omega) I_0(\Omega) \mathrm{d}\Omega} \right). \tag{5}$$

Assuming I_0 doesn't vary greatly across the sky, and voxelizing the field of view of the riometer, equation (5) can be written as

$$\text{Absorption} = -10 \log_{10} \left(\frac{\sum_{i=1}^{I} G_i \Delta\Omega_i \exp\left(-2 \sum_{j=1}^{J} \kappa_j l_{ij} \right)}{\sum_{i=1}^{I} G_i \Delta\Omega_i} \right). \tag{6}$$

The integral over solid angle, is numerically represented by a summation of solid angle $\Delta\Omega_i$ for a set of ray directions i, with gain G_i. The ray directions are evenly spaced over all directions from the riometer in steps of 2 degrees in zenith and azimuth, giving 8100 rays. κ_j represents the absorption coefficient in voxel j. l_{ij} is the intersect length of ray i with voxel j. Equation (6) clearly shows that this is not a linear problem, therefore linear tomographic methods used in many tomographic applications will not work and a nonlinear method will have to be implemented.

3.2.2. Occam's Inversion

[14] Occam's inversion is a popular method for solving nonlinear inversion problems and was first introduced by *Constable et al.* [1987]. The inversion is an iterative algorithm which searches for the smoothest fit to the model $H(\kappa)$, subject to an appropriate fit to the data. This can be represented as

$$\min\{\| WH(\kappa) - Wd \|^2 - \alpha \| L(x) \|^2\}. \tag{7}$$

This is similar to Tikhonov regularization of linear inversion problems [*Aster et al.*, 2005]. Alpha represents the regularization parameter, $\alpha > 0$. $H(\kappa)$ is the forward model, equation (6) described in section 3.2.1. d is the data vector (absorption values for IRIS and ARIES). W is the diagonal matrix of weighting factors of the data.

$$W = diag\{1/\sigma_1, 1/\sigma_2, \cdots 1/\sigma_X\}. \tag{8}$$

These are the data variances of the beams given by 0.05 for IRIS and 0.3 for ARIES. The difference in weighting factors stops the ARIES data dominating over the IRIS data. L is the roughening matrix which takes different forms for different orders of regularization. For zero order regularization L=I, where I is the identity matrix. L is implemented to be 3-D finite difference solution of the laplacian for κ, given by

$$\begin{aligned}\nabla^2\kappa(x,y,z) = \frac{1}{h^2}[&\kappa(x+h,y,z) + \kappa(x-h,y,z) + \kappa(x,y+h,z)\\ &+ \kappa(x,y-h,z) + \kappa(x,y,z+h)\\ &+ \kappa(x,y,z-h) - 6\kappa(x,y,z)].\end{aligned} \tag{9}$$

This constrains κ to be smooth in the x, y and z directions (longitude, latitude and altitude). A starting value of $\kappa = 0.001$ for all voxels is used to start the iteration process. (k=1, where k is the iteration number). The iteration of κ is performed by use of equation (10).

$$\kappa^{k+1} = \left(\left(WJ\left(\kappa^k\right)\right)^T WJ\left(\kappa^k\right) + \alpha^2 L^T L\right)^{-1}\left(WJ\left(m^k\right)\right)^T \hat{d}\left(\kappa^k\right). \tag{10}$$

J is the Jacobian matrix of κ. $\hat{d}$ is

$$\hat{d}\left(\kappa^k\right) = d - H\left(\kappa^k\right) + J\left(\kappa^k\right)\kappa^k. \tag{11}$$

The goodness of fit between the model and data is assessed using the χ^2 least squares criteria

$$\chi^2 = \sum (WH(\kappa) - Wd)^2. \tag{12}$$

Unlike many regularization regimes where α is constant and set before the optimization, Occam's inversion dynamically adjusts α at each iteration so that the χ^2 value of the solution does not exceed a threshold value (δ). If a value does not exist, the α that minimizes the solution most is chosen. It is assumed that the noise on the data is uncorrelated and due to a Gaussian process then δ is the number of data points [*deGroot-Hedlin and Constable*, 1990]. The drawback to this method that it allows negative values for κ, where in reality negative absorption does not occur. A full description of the Occam's inversion algorithm can be found by *Constable et al.* [1987] and *Aster et al.* [2005].

3.3. Vertical Parallax Technique

[15] *Terkildsen et al.* [2004] developed the vertical parallax method to estimate the height of greatest CNA. The vertical parallax method calculates the time lag between observing a moving patch of absorption in a single beam of one imaging riometer, and the same event in an intersecting beam of the second riometer. The relationship between the time lag and height of the absorption event is

$$T = \left(\frac{H - Z}{Z}\right)\frac{L}{V}. \tag{13}$$

where V is apparent velocity of the absorption patch between the two instruments, H is event altitude, Z is altitude of the beam intersection and L is horizontal distance between the two riometers. Plotting time lag against beam intersection altitude will allow calculation of the event altitude. Fitting a curve to the result, where the curve passes through 0 time lag is the event altitude. Only beam-pair cross correlations of 0.9 or greater are used in this study. For a full description of the vertical parallax method see *Terkildsen et al.* [2004].

[16] The assumptions and requirements for the vertical parallax method to work are; first the absorption patch moves across the field of view of the two imaging riometers. Second over the segments of the event (a moving feature) the height of the absorption event doesn't change.

4. Test Data

[17] Using the forward model described in section 3.2.1 it is possible to create data with which to test the height triangulation, vertical parallax and 3-D reconstruction methods. Such data are refereed to as phantoms in tomographic literature, such as *Fougere* [1995] and we follow this convention here. Figure 3 shows three test phantoms. Phantom A is a layer of absorption at 100 km. Phantom B is an "arc" along 69.3° latitude, at 85 km, with a Gaussian profile in the vertical and longitudinal direction. Phantom C is a patch of absorption at 90 km altitude; location 69.5°N, 19.5°E. Each phantom has a peak of 0.001 dB/m. The reconstructed phantoms are seen on the right of Figure 3. Figure 4 shows a vertical profile of the phantoms taken through the center of each absorption patch phantom.

[18] Figure 5 shows the results of the height triangulation on the phantoms. The height triangulation is able to triangulate the height for both phantom B and C. Unsurprisingly it cannot calculate the height of maximum CNA for phantom A, as phantom A is a diffuse layer, with no spatial features.

[19] Modifying the arc and patch phantoms to move in time across the field of view of the riometers the vertical parallax method can also be tested. The two phantoms are modified to move across 1° in latitude at a speed of $0.01°\ s^{-1}$ over the field of view of the riometers. Figure 6a shows the lag-height result for the arc phantom, while Figure 6b shows the result for the patch. The plot shows the lag time of absorption observed by intersecting beams of ARIES and IRIS as a function of their intersection height. The heights of maximum CNA are correctly found using this method.

5. Comparison Between Height Triangulation, Vertical Parallax and Tomographic Method

[20] Table 1 shows the results of the three height routines on the three test phantoms. The best results are from the tomographic reconstruction which estimates the height of maximum CNA for all three test phantoms. However the reconstruction underestimates and smooths the absolute values. Both the height triangulation and vertical parallax method reconstruct the height of peak CNA for two out of

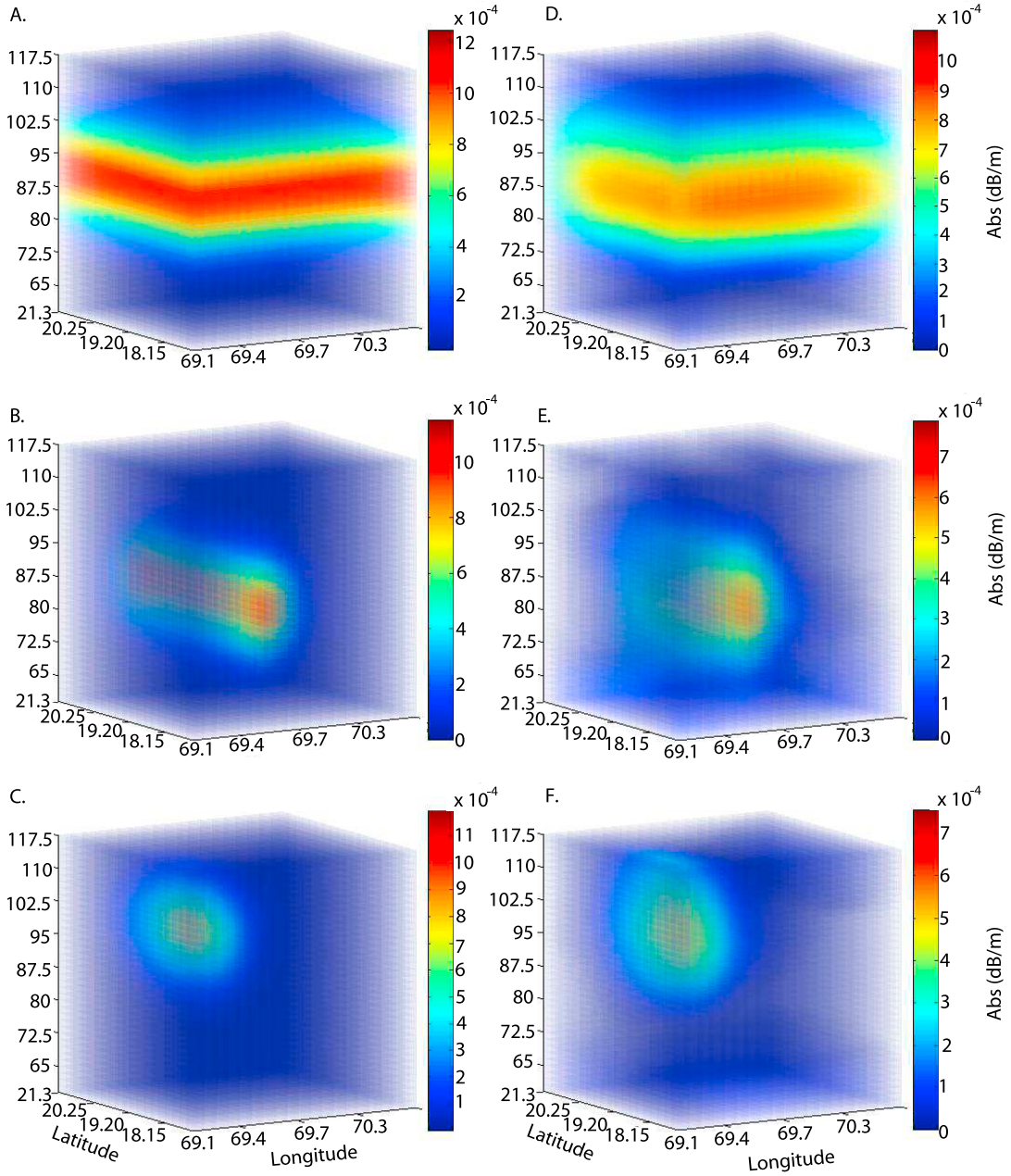

Figure 3. (left) Phantom data created to test inversion. (a) "Layer" at 90 km. (b) "Arc" at 85 km, along 69.3° (0.1° width) latitude. (c) Absorption patch with Gaussian form in longitude, latitude, and height at 100 km (69.5°N, 19.5°E, with widths of 0.1° and 0.9°, respectively). All phantoms have a max CNA of 0.001 dB/m and vertical extent of 8 km. (right) Reconstructed images of the three phantoms using Occam's inversion. (d) Layer. (e) Gaussian arc. (f) Gaussian patch.

three of the phantoms. However looking at the assumptions and requirements for each method, the new height triangulation method has advantages over the vertical parallax method. First the vertical parallax method can only measure one value for the height of max CNA over a segment of the event (a moving feature), with events lasting from minutes to tens of minutes; whereas the height triangulation method can measure the rapidly changing absorption structure of the order of tens of seconds (this resolution allows for noise in the data to be averaged out). Second the vertical parallax method has the requirement of a moving absorption patch; an assumption not required for the height triangulation method. The height triangulation method can calculate the height estimates for an absorption event relatively quickly (30 s to 1 min) compared to the tomographic method (3–5 min). However the height triangulation assumes the absorption event occurs at a constant height across the field of view, an assumption that the tomographic method does not require.

[21] The tomographic reconstruction and height triangulation offer improvements over the vertical parallax method,

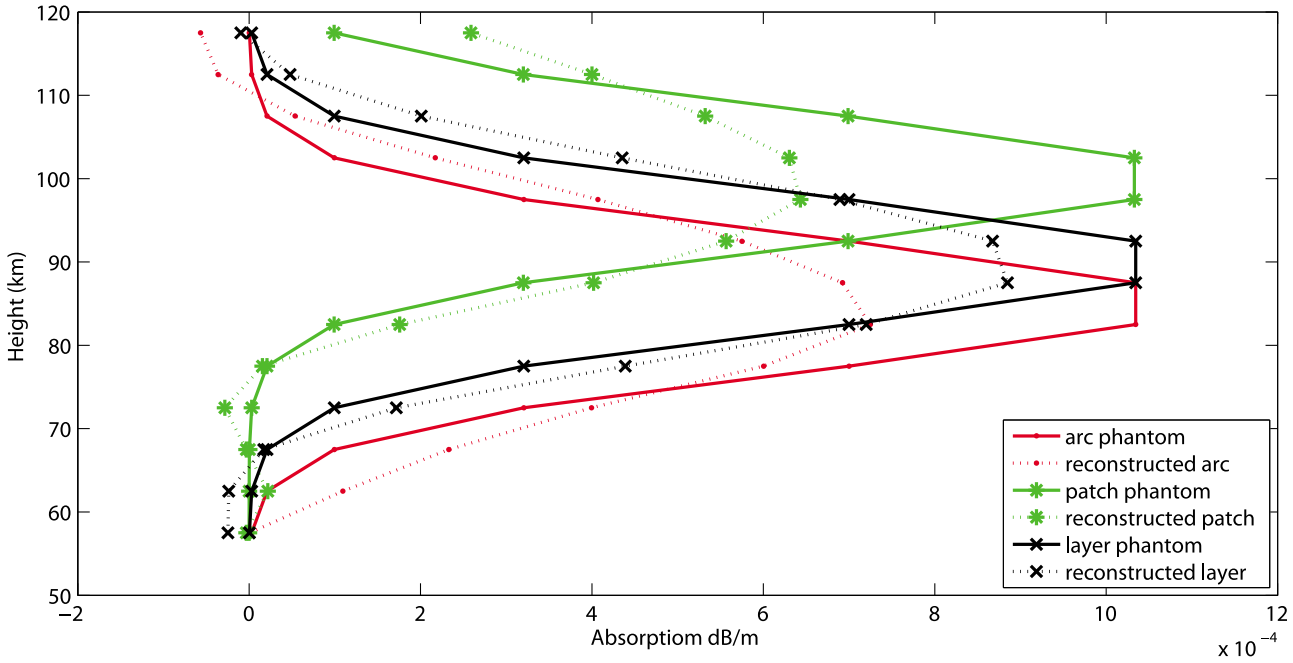

Figure 4. Vertical absorption profiles for phantom and reconstructed absorption objects. Solid lines are phantoms through location of greatest absorption. Dotted lines show reconstructed artifacts. Red (dots), arc; green (stars), patch; black (crosses), layer.

with the tomographic reconstruction offering the greatest versatility.

6. Comparison With EISCAT

[22] Between 14 and 24 UT on the 22 May 2008 the EISCAT VHF antenna was running the "beata" program. This program measures electron densities down to the lower D region. For this run the antenna was pointing near vertical. The electron density profile measured by EISCAT is converted to an absorption profile by the use of the equation below [*Hargreaves*, 1969],

$$A = 4.6 \times 10^{-5} \int \frac{n\nu dl}{\nu^2 + (\omega \pm \omega_H \cos\theta)^2}. \qquad (14)$$

A is the absorption in dB, n is the electron density (m^{-3}), ν is the effective electron collision frequency, ω_H is the electron gyrofrequency, ω is the frequency of the attenuated wave, and finally θ is the angle between the magnetic field and the propagating wave. It is assumed that the absorbed radio wave propagates nearly parallel to the magnetic field lines so the angle is 0° and X mode is selected to match observations.

[23] Figure 7b shows this absorption profile. The height of maximum CNA as measured by EISCAT and calculated by the height triangulation and tomographic methods are shown in panel 4. The vertical parallax method failed to produce any results. During the absorption event between 19:00 UT and 19:30 UT the correlation between the three measurements falls within errors, estimating it to be on average 74 ± 5 km. The height triangulation and tomography also reconstruct the absorption event between 21:45 UT and 22:15 UT.

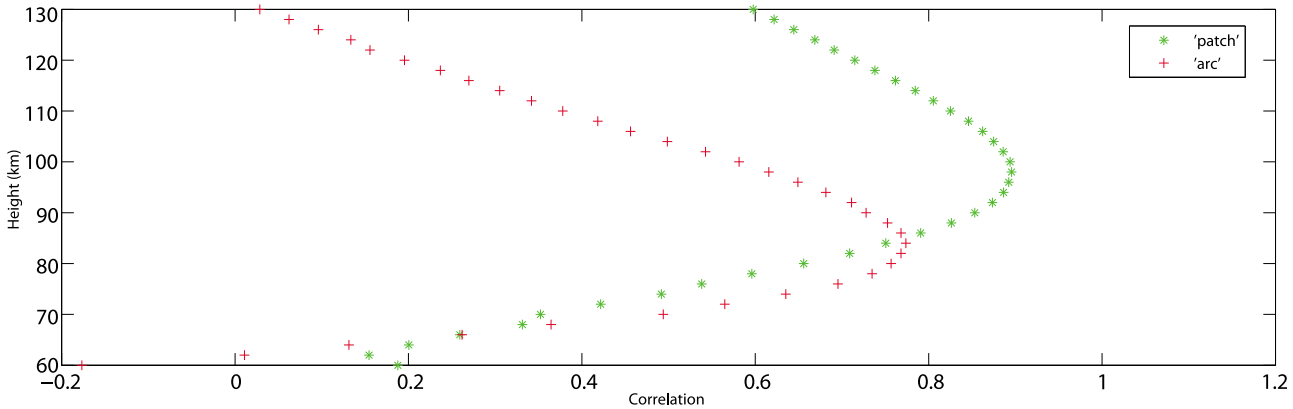

Figure 5. Height versus correlation for the three phantoms using the height triangulation method.

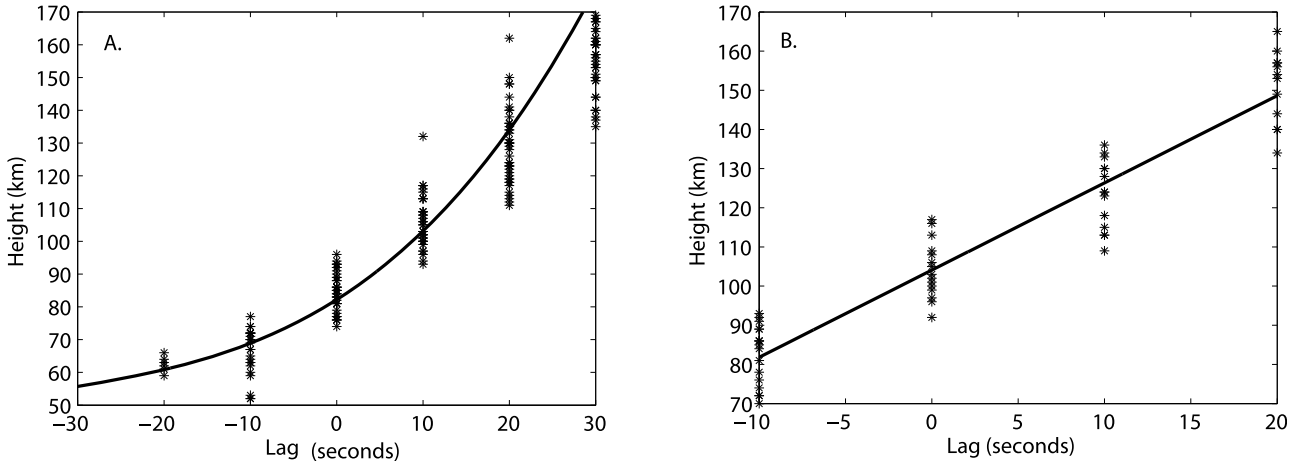

Figure 6. Vertical parallax method for arc and patch phantom. Phantom been modified to move 1° in latitude at a speed of 0.01° s^{-1}. The plots show the lag time of observed absorption between intersecting ARIES and IRIS beams versus the intersection height of the beams. (a) Time lag versus height for arc at 80 km. (b) Time lag versus height for patch at 100 km.

Between 19:40 and 19:50 UT EISCAT observes a patch of absorption that none of the height estimation techniques can pick out. One possibility for this omission could be that this is a small-scale event that cannot be resolved by the techniques. Figure 7c shows absorption plots of IRIS beam 9 and ARIES beam 656. These two beams intersect at 71 km. Between 19:00 and 19:40 UT, they show a similar pattern of absorption, consistent with the tomography and height triangulation results that indicate the height of peak CNA is 75 km. Between 19:40 and 20:00 UT ARIES records lesser absorption, consistent with the EISCAT absorption values given the geometry of the overlapping IRIS, ARIES and EISCAT beams. The larger beam width (and hence vertical extent) of IRIS explains why it observes absorption at that time.

7. Estimating the Characteristic Energy

[24] Estimates of the characteristic energy of the precipitating electrons are obtained by relating the height of maximum CNA to an assumed flux spectrum ϕ. Absorption is related to electron density by equation (14). The steady state ion production rate is given by $q = \alpha n^2$ [*Semeter and Kamalabadi*, 2005], or $n = \sqrt{q/\alpha}$, where n is the ion density, and α is the effective recombination rate. Equation (14) can be rewritten in terms of the ion production rate.

$$A = 4.6 \times 10^{-5} \int \frac{\sqrt{q/\alpha}\nu dl}{\nu^2 + (\omega \pm \omega_H \cos\theta)^2}, \tag{15}$$

q is a function of ϕ. *Semeter and Kamalabadi* [2005] give a comprehensive description of calculating q. Various flux spectra can be used to describe the distribution of incoming electrons. A Maxwellian spectrum is used for this paper, given by

$$\phi(E) = \frac{Q_0}{2E_C^3} E \exp\left(-\frac{E}{E_c}\right), \tag{16}$$

ϕ is the number flux directed in the downward direction for an isotropic distribution of electrons ($m^{-2}\ s^{-1}\ eV^{-1}$). Q_0 is the total energy flux (eV $m^{-2}\ s^{-1}$), E_c is the characteristic energy (eV) and E is the energy of the electrons (eV). A value of 6.452×10^{15} (eV $m^{-2}\ s^{-1}$) for the total energy flux, this is 1 mW/m^2, a convention used in papers such as *Senior et al.* [2007] is used. To relate the height of maximum CNA to characteristic energy, absorption profiles are calculated using equation (15), calculating the ion production rate by the method set out by *Semeter and Kamalabadi* [2005]; using values between 1 keV and 300 keV for the characteristic energy.

[25] ν is a sum of the electron-ion and electron-neutral collisions. Both are taken from *Schunk and Nagy* [1978]. Values for the ion and neutral species and temperatures are needed to calculate the collision frequencies. These are taken from the International Reference Ionosphere; IRI-2001 [*Bilitza*, 2001] and MSIS90 [*Hedin*, 1991].

[26] The main source of uncertainty though comes from the choice of effective recombination rate α. In this study two recombination rates are used, one from *del Pozo et al.* [1997] and one from *Vickrey et al.* [1982] to give an estimation of the boundary values for the characteristic energy.

$$\alpha = 2.5 \times 10^{-6} \exp(-0.0242h) + 1.63 \times 10^{11} \exp(-0.524h) \tag{17}$$

$$\alpha = 2.5 \times 10^{-6} \exp(-h/51.2); \tag{18}$$

α is the effective recombination rate ($cm^3\ s^{-1}$), h is the height in kilometers. Equation (17) is used when the height of peak

Table 1. Results From the Three Height Estimation Routines for the Three Test Phantoms

Height Method	Patch	Arc	Layer
Tomographic	Yes	Yes	Yes
Height Triangulation	Yes	Yes	No
Vertical Parallax	Yes	Yes	No

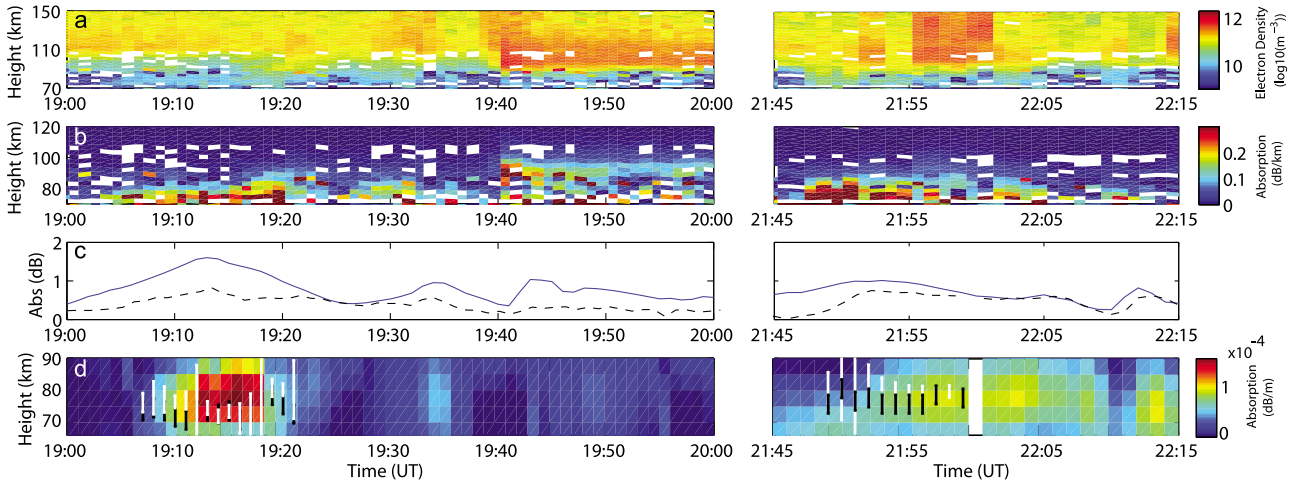

Figure 7. From top to bottom: (a) EISCAT Electron density. (log10(m^{-3})). (b) Absorption profile using EISCAT electron density (dB/km). (c) Absorption in beam 9 of IRIS (solid line) and beam 656 of ARIES (dashed line) (dB). These beams intersect at 71 km. (d) Vertical absorption profiles using the tomographic method (69.5° latitude, 19.2° longitude) with the peak height of CNA marked on in black from EISCAT. Error bars generated using the length of the range gate. Height triangulation method is marked in white (only cross-correlation values over 0.6), 22 May 2008, 19:00–22:30 UT. Between 20:00 UT and 21:45 UT is not shown as there was no activity.

CNA is over 80 km while equation (18) is used for events below 80 km.

8. Case Studies

[27] In this section we apply the height triangulation and tomographic technique to three different types of CNA to examine the differences in deposition height. The vertical absorption profiles from the tomographic methods are averaged to give a mean absorption profile for the field of view. Each event is similar to one of the phantoms discussed in section 3.

8.1. Substorm Spike Event

[28] On 23 December 2007 there was a period of sustained negative Bz of around −1 nT in the interplanetary magnetic field (IMF) as identified by OMNI data set. This provided low but sustained coupling of the IMF to the magnetosphere and led to the onset of a substorm at 21:20 UT, observed by the IMAGE magnetometer chain. Figure 8 shows data for the event in question. Figure 8a shows a 100 nT negative bay in the X component from the Kilpisjärvi magnetometer. IRIS measured an absorption spike [e.g., *Aminaei et al.*, 2006] in the northwest quadrant of its field of view. Figure 8b shows the absorption in beam 9 of IRIS between 21:15 and 21:30 UT with the corresponding height estimates shown in Figure 8c; the duration of the spike was 5 min. As the event progresses the height triangulation method show a decrease in peak altitude from 100 ± 3 km to 92 ± 3 km where there is a local maximum in total absorption of 1.4 dB. The tomographic method shows a more constant height across the event at 95 ± 3 km which then decreases height to 85 ± 3 km as the event continues. The characteristic energy changes from 5 keV to a peak of 14–15 keV. This variation indicates a rapid hardening of the electron spectrum during the spike event in agreement with other studies [*Collis and Hargreaves*, 1997] and suggests that the CNA associated with the spike is formed by the energetic tail of auroral electrons. Three absorption images in Figure 8 show the evolution of the CNA patches; at 21:21 UT there is a discrete patch which increases in magnitude as the event progresses. By 21:22 UT there are two distinct patches in the field of view. This is also the time at which the height estimation technique breaks down.

8.2. Slowly Varying Absorption (SVA)

[29] Figure 9a shows an example of slowly varying absorption; a common feature in the auroral zone, characterized by a smooth increase and decrease in the CNA over a period of a few hours [*Devlin et al.*, 1986]. This example is from the 4 October 2007 when there was a long period of CNA between 03:30 and 06:30 UT. This is likely generated by electrons gradient-curvature drifting eastward in the magnetosphere and precipitating via interaction with whistler mode chorus waves. During the onset (03:30–04:00 UT) of absorption the height of maximum CNA is 82 ± 5 km (Figure 9b). Figure 9 (top) shows how the event progressed with a discrete structure becoming steadily more diffuse. The height triangulation breaks down over the course of this transition; as the CNA becomes more diffuse the error on the height increases to ±20 km, whereas the tomographic method still reconstructs the event, showing an increase in the height to around 87 ± 3 km. This structure is similar to the stratified layer discussed in section 3, where the height triangulation method also failed to work due to its diffuse nature. Estimates of the characteristic energy for the period between 3:30 UT and 3:45 UT is 18–20 keV. The energy is larger than for the substorm spike in agreement with past studies [e.g., *Osepian et al.*, 1996].

8.3. Afternoon CNA Spike

[30] Figure 10 shows data from IRIS and ARIES for a short duration (4 min) spike at 14:57 UT on 4 October 2007. Local magnetometer recorded no disturbance and this event cannot be explained as a sudden commencement effect. One possibility is that this event is an example of a high-latitude absorption

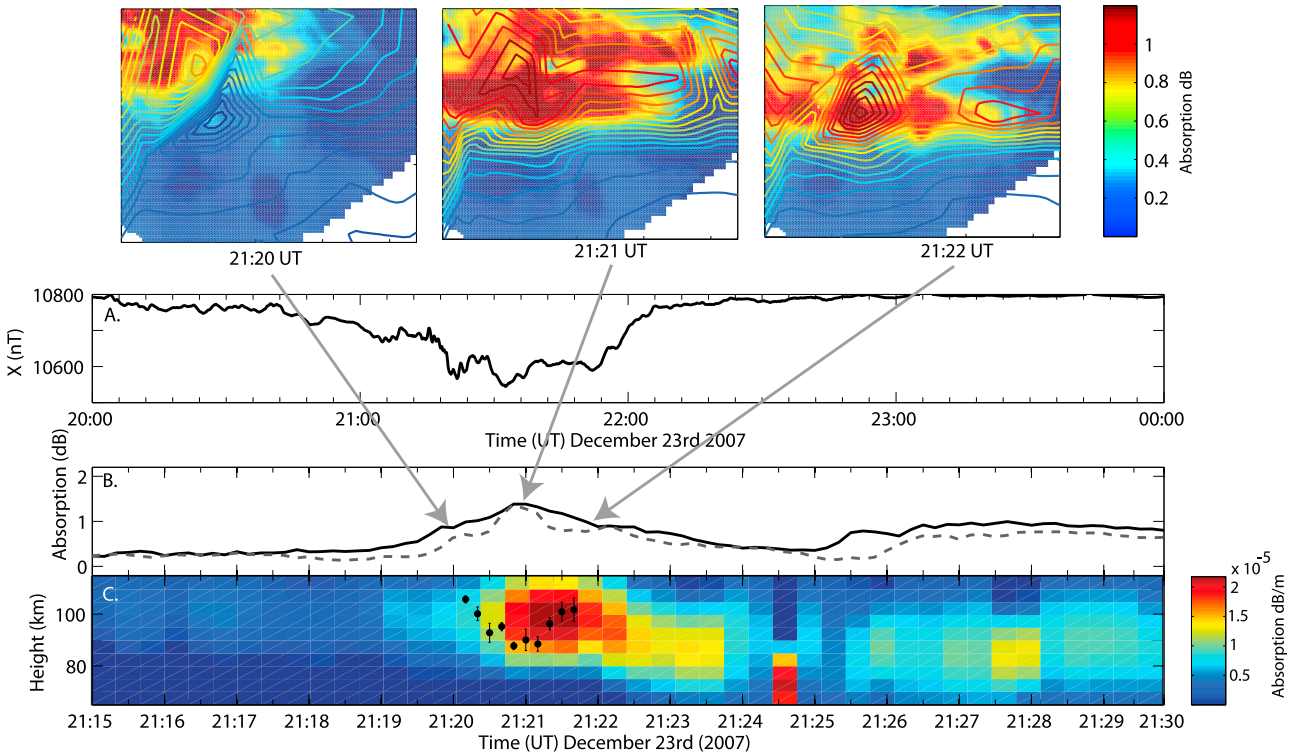

Figure 8. Plot for absorption event on the 23 December 2007. (top) ARIES absorption images with IRIS contour plot overlaid projected to a height of 90 km. (a) The X component of the IMAGE magnetometer at Kilpisjärvi between 20:00 and 00:00 UT. (b) Absorption between 21:15 and 21:30 UT for beam 9 in IRIS (solid line) and beam 560 in ARIES (dashed line) (dB). These two beams intersect at 85 km. (c) Mean absorption profiles using the tomographic method, with the height of maximum CNA using the height triangulation marked on in black (cross-correlation values over 0.6).

spike [*Ranta et al.*, 1997]. These events are short-lived with relatively low absorption (<1 dB), exhibiting horizontal structure of ~180 by 130 km at 90 km altitude [*Ranta et al.*, 1997]. Figure 10b shows the height estimates of this absorption event, which is centered around 75 ± 5 km according to the height triangulation and tomographic method. The absorption images in Figure 10 show an arc like structure that moves across the field of view. This is similar in shape to the arc phantom in section 3. The exact cause of these spikes is unknown but it has been suggested to be due to scattering of high-energy electrons by EMIC waves [e.g., *Ranta et al.*, 1997; *Clilverd et al.*, 2007]. Since EMIC waves are known to resonate with electrons having energies greater than 100 keV [*Horne and Thorne*, 1998] the CNA would have to be generated by much higher-energy electrons than in other events. This high energy supports the fact that these events occur at lower heights compared to the other two cases. More accurate estimates of the characteristic energy cannot be specified for this event since at this altitude the composition of the ionosphere is more complicated, with greater inaccuracies in the recombination rate, coupled with the fact that the distribution of incoming electrons is largely unknown, meaning a Maxwellien spectrum may not be the best choice.

9. Conclusions

[31] This paper presents a comprehensive comparison of methods to estimate the height of auroral absorption events using two riometers. We found that both the height triangulation and tomographic method offer significant improvements over the vertical parallax method for IRIS-ARIES observations. The tomographic method provides an estimate of the height of peak CNA at the expense of the exact values of the internal CNA. The required smoothing of the differential absorption values retains the shape of the absorption profile but leads to an unavoidable underestimate of the integral value. This can be seen in the test phantoms. The height triangulation and tomographic methods described are successfully employed on real absorption data. Comparison with absorption plots created from electron density measurements from the EISCAT mainland radar show for this case that the height triangulation and tomographic method work for the majority of the events. The height triangulation works for discrete, single patches of absorption, however its validity is questionable when absorption is too diffuse or has multiple patches at different altitude in the field of view. This is represented in the height triangulation normally with a cross correlation value of less than 0.6. The height triangulation and tomographic methods offer an improvement over previous methods [*Terkildsen et al.*, 2004], with ability to work on more absorption types, and give estimates on the height of maximum CNA to a resolution of ~10 s.

[32] The height triangulation and tomographic methods were applied to three case studies; a spike at substorm onset, slowly varying absorption, and a daytime absorption spike. Application of the vertical parallax method were not possible

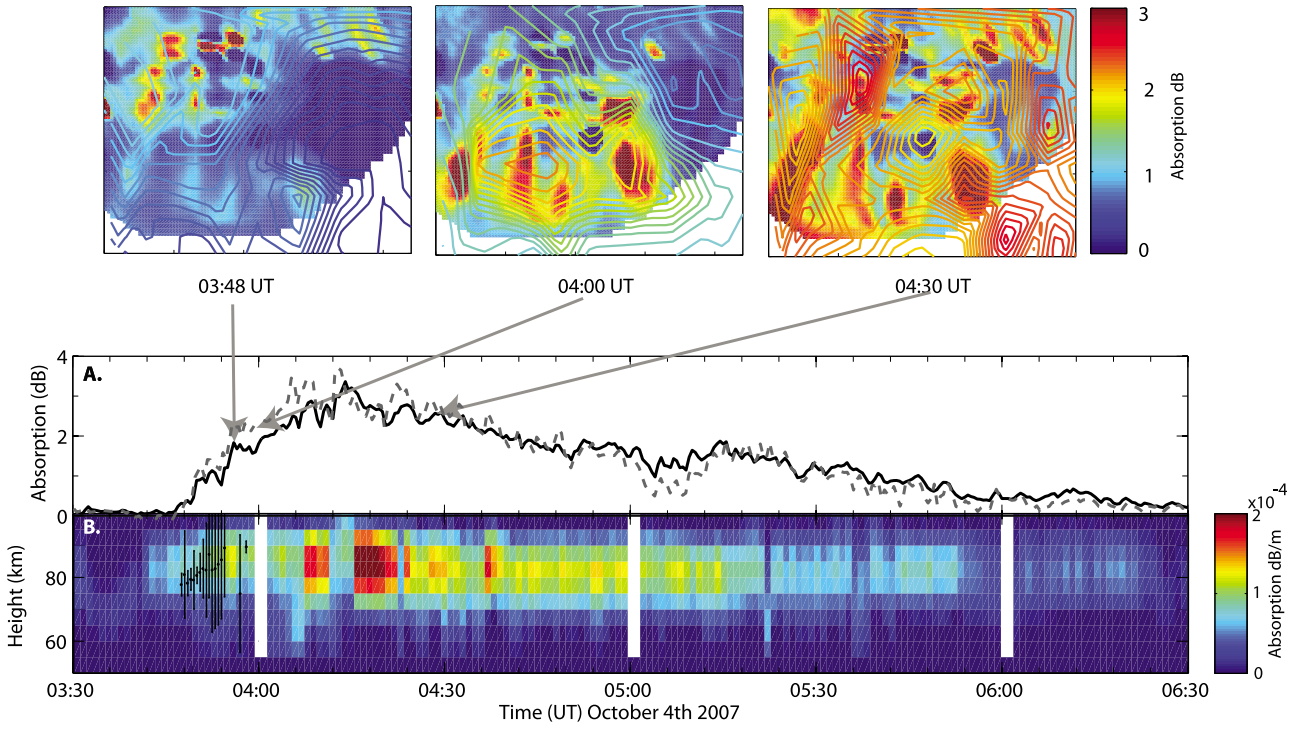

Figure 9. Plot for absorption event on the 4 October 2007. (top) ARIES absorption images with IRIS contour plot overlaid projected to a height of 85 km (dB). (a) shows absorption between 03:30 and 06:30 UT in beam 25 of IRIS (solid line) and beam 792 of ARIES (dashed line) (dB). These beams intersect at 80 km. (b) Mean absorption profiles using the tomographic method, with the height of maximum CNA using the height triangulation marked on in black (cross-correlation values over 0.6).

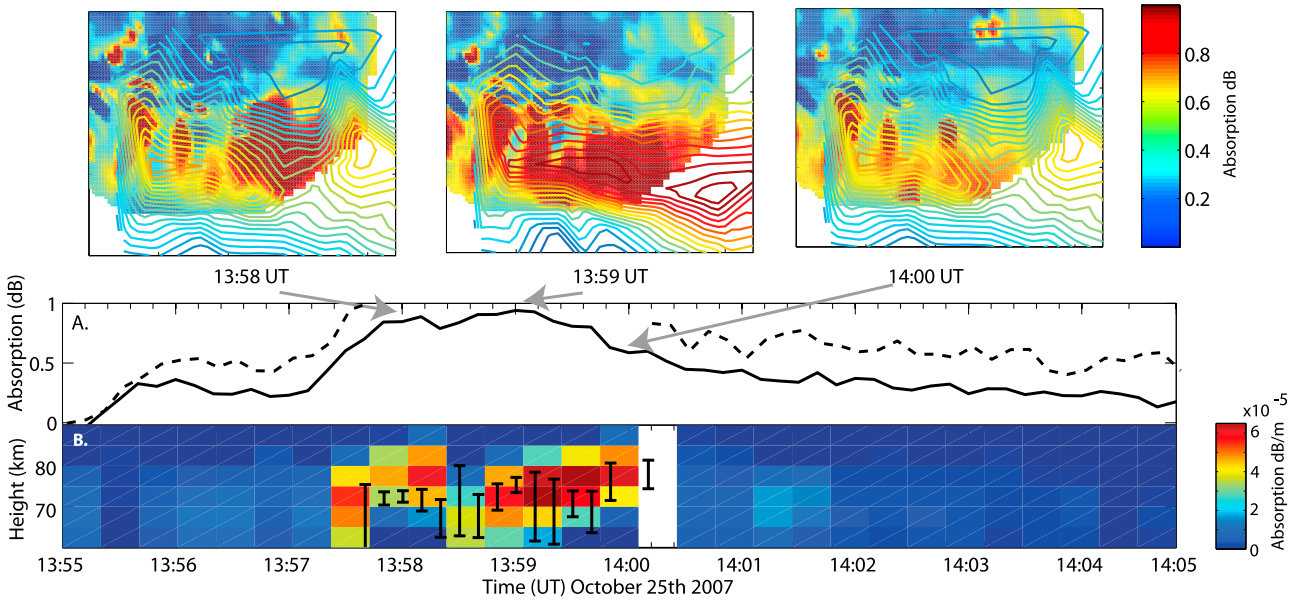

Figure 10. Plot for absorption event on 25 October 2007. (top) ARIES absorption images with IRIS contour plot overlaid projected to a height of 75 km (dB). (a) Absorption between 14:55 and 15:05 in beam 25 of IRIS (solid line) and beam 824 of ARIES (dashed line) (dB). These beams intersect at 72 km. (b) Mean absorption profiles using the tomographic method, with the height of maximum CNA using the height triangulation marked on in black (cross correlation values over 0.6).

on the three case studies. This is due to the fact that for each case study the absorption patch did not move across the field of view and keep a constant structure for time scales required for successful height estimates using this method. The tomographic method agreed with the height triangulation method for each event.

[33] Applying an assumed Maxwellian spectrum, estimates of the characteristic energy using the height of maximum CNA were done. The values for the characteristic energy for the substorm spike was 5 keV and the beginning of the slowly varying absorption at 18–20 keV. The energy of the afternoon spike event could not be calculated accurately using the model, due to the very low altitude of absorption, but it did indicate the electrons had a characteristic energy greater than 100 keV. This fits with the theory of a daytime absorption spike, as they are thought to be due to electrons with very large energies.

[34] **Acknowledgments.** Riometer data originated from the Imaging Riometer for Ionospheric Studies (IRIS), operated by the Department of Communications Systems at Lancaster University (UK) in collaboration with the Sodankylä Geophysical Observatory, and funded by the Science and Technology Facilities Council (STFC) and the Advanced Rio-Imaging Experiment in Scandinavia (ARIES), operated by the Department of Communications Systems at Lancaster University (UK) and funded by the Science and Technology Facilities Council (STFC). EISCAT is an international association supported by research organizations in China (CRIRP), Finland (SA), France (CNRS, till end 2006), Germany (DFG), Japan (NIPR and STEL), Norway (NFR), Sweden (VR), and the United Kingdom (STFC). Magnetometer data were taken from the International Monitor for Auroral Geomagnetic Effects (IMAGE). We thank the institutes who maintain the IMAGE Magnetometer Array. P. Wild is supported by a STFC studentship.

[35] Robert Lysak thanks Peter Stauning and another reviewer for their assistance in evaluating this paper.

References

Aminaei, A., F. Honary, A. J. Kavanagh, E. Spanswick, and A. Viljanen (2006), Characteristics of nighttime absorption spike events, *Ann. Geophys.*, *24*(7), 1887–1904, doi:10.5194/angeo-24-1887-2006.

Arnoldy, R. L., and K. W. Chan (1969), Particle substorms observed at the geostationary orbit, *J. Geophys. Res.*, *74*(21), 5019–5028, doi:10.1029/JA074i021p05019.

Ashrafi, M., and M. Kosch (2004), Height triangulation of artificial optical emissions in the f layer, in *Proceedings of the 31st Annual European Meeting on Atmospheric Studies by Optical Methods, and 1st International Riometer Workshop, 22–28 Aug.*, edited by M. J. Kosch, Lancaster Univ., Ambleside, U. K.

Aster, R., B. Borchers, and H. Clifford (2005), *Parameter Estimation and Inverse Problems*, Elsevier, New York.

Bhuyan, K., S. Singh, and P. Bhuyan (2002), Tomographic reconstruction of the ionosphere using generalized singular value decomposition, *Curr. Sci.*, *83*(9), 1117–1120.

Bilitza, D. (2001), International reference ionosphere 2000, *Radio Sci.*, *36*(2), 261–275, doi:10.1029/2000RS002432.

Browne, S., J. K. Hargreaves, and B. Honary (1995), An imaging riometer for ionospheric studies, *Electron. Commun. Eng. J.*, *7*(5), 209–217, doi:10.1049/ecej:19950505.

Clilverd, M. A., C. J. Rodger, R. M. Millan, J. G. Sample, M. Kokorowski, M. P. McCarthy, T. Ulich, T. Raita, A. J. Kavanagh, and E. Spanswick (2007), Energetic particle precipitation into the middle atmosphere triggered by a coronal mass ejection, *J. Geophys. Res.*, *112*, A12206, doi:10.1029/2007JA012395.

Collis, P., and J. Hargreaves (1997), Co-ordinated studies using imaging riometer and incoherent scatter radar, *J. Atmos. Sol. Terr. Phys.*, *59*(8), 873–890, doi:10.1016/S1364-6826(96)00062-4.

Constable, S., R. Parker, and G. Constable (1987), Occam's inversion: A practical algorithm for generating smooth models from electromagnetic sounding data, *Geophysics*, *52*, 289–300, doi:10.1190/1.1442303.

deGroot-Hedlin, C., and S. Constable (1990), Occam's inversion to generate smooth, two-dimensional models from magnetotelluric data, *Geophysics*, *55*, 1613, doi:10.1190/1.1442813.

del Pozo, C., J. Hargreaves, and A. Alyward (1997), Ion composition and effective recombination rate in the nighttime auroral lower ionosphere, *J. Atmos. Sol. Terr. Phys.*, *59*(15), 1919–1943, doi:10.1016/S1364-6826(97)00033-3.

Detrick, D., and T. Rosenberg (1990), A phased array radio wave imager for studies of cosmic noise absorption, *Radio Sci.*, *25*(4), 325–338, doi:10.1029/RS025i004p00325.

Devlin, T., J. Hargreaves, and P. Collis (1986), Eiscat observations of the ionospheric d region during auroral radio absorption events, *J. Atmos. Sol. Terr. Phys.*, *48*(9–10), 795–805, doi:10.1016/0021-9169(86)90054-1.

Fougere, P. (1995), Ionospheric radio tomography using maximum entropy: I. Theory and simulation studies, *Radio Sci.*, *30*(2), 429–444, doi:10.1029/94RS03164.

Grill, M. (2007), Technological advances in imaging riometry, Ph.D. thesis, Lancaster Univ., Lancaster, U. K.

Gustavsson, B. (2000), Three-dimensional imaging of aurora and airglow, Ph.D. thesis, Swedish Inst. Space Phys., Kiruna, Sweden.

Hargreaves, J. (1969), Auroral absorption of hf radio waves in the ionosphere: A review of results from the first decade of riometry, *Proc. IEEE*, *57*(8), 1348–1373, doi:10.1109/PROC.1969.7275.

Hedin, A. E. (1991), Extension of the msis thermospheric model into the middle and lower atmosphere, *J. Geophys. Res.*, *96*(A2), 1159–1172, doi:10.1029/90JA02125.

Honary, F., P. Chapman, M. Grill, K. Barratt, S. Marple, E. Nielsen, and T. Hagfors (2005), Advanced rio-imaging experiment in scandinavia (aries): System specification and scientific goals, in *Proceedings of the URSI XXVIII General Assembly*, New Delhi, India.

Horne, R. B., and R. M. Thorne (1998), Potential waves for relativistic electron scattering and stochastic acceleration during magnetic storms, *Geophys. Res. Lett.*, *25*(15), 3011–3014, doi:10.1029/98GL01002.

Kavanagh, A. J., M. Kosch, F. Honary, A. Senior, S. R. Marple, E. E. Woodfield, and I. W. McCrea (2004), The statistical dependence of auroral absorption on geomagnetic and solar wind parameters, *Ann. Geophys.*, *22*, 877–887, doi:10.5194/angeo-22-877-2004.

Kavanagh, A. J., G. Lu, E. Donovan, G. Reeves, F. Honary, J. Manninen, and T. Immel (2007), Energetic electron precipitation during sawtooth injections, *Ann. Geophys.*, *25*, 1199–1214, doi:10.5194/angeo-25-1199-2007.

Little, C., and H. Leinbach (1959), The riometer-a device for the continuous measurement of ionospheric absorption, *Proc. IRE*, *47*, 315–320.

Marple, S., and F. Honary (2004), A multi-instrument data analysis toolbox, *Adv. Polar Upper Atmos. Res.*, *18*, 120–130.

Osepian, A., S. Kirkwood, and N. Smirnova (1996), Energetic electron precipitation during auroral events observed by incoherrent scatter radar, *Adv. Space Res.*, *17*(11), 149–155, doi:10.1016/0273-1177(95)00743-X.

Ranta, H., A. Ranta, J. Hargreaves, and S. Browne (1997), Localized absorption events in the afternoon sector, *J. Atmos. Sol. Terr. Phys.*, *59*(8), 891–902, doi:10.1016/S1364-6826(96)00063-6.

Rees, M. (1989), *Physics and Chemistry of the Upper Atmosphere*, Cambridge Univ. Press, Cambridge, U. K.

Rishbeth, H., and A. van Eyken (1993), Eiscat: Early history and the first ten years of operation, *J. Atmos. Sol. Terr. Phys.*, *55*(4–5), 525–542, doi:10.1016/0021-9169(93)90002-G.

Schunk, R. W., and A. F. Nagy (1978), Electron temperatures in the *F* region of the ionosphere: Theory and observations, *Rev. Geophys.*, *16*(3), 355–399, doi:10.1029/RG016i003p00355.

Semeter, J., and F. Kamalabadi (2005), Determination of primary electron spectra from incoherent scatter radar measurements of the auroral E region, *Radio Sci.*, *40*, RS2006, doi:10.1029/2004RS003042.

Semeter, J., and M. Mendillo (1997), A nonlinear optimization technique for ground-based atmospheric emission tomography, *IEEE Trans. Geosci. Remote Sens.*, *35*, 1105–1116, doi:10.1109/36.628779.

Senior, A., A. J. Kavanagh, M. J. Kosch, and F. Honary (2007), Statistical relationships between cosmic radio noise absorption and ionospheric electrical conductances in the auroral zone, *J. Geophys. Res.*, *112*, A11301, doi:10.1029/2007JA012519.

Stauning, P. (1996), Investigations of ionospheric radio wave absorption processes using imaging riometer techniques, *J. Atmos. Sol. Terr. Phys.*, *58*(6), 753–764, doi:10.1016/0021-9169(95)00072-0.

Terkildsen, M., B. Fraser, and H. Yamagishi (2004), Determination of the altitude peak of cosmic noise absorption using a vertical parallax technique, *Geophys. Res. Lett.*, *31*, L07802, doi:10.1029/2003GL019068.

Vickrey, J. F., R. R. Vondrak, and S. J. Mathews (1982), Energy deposition by precipitating particles and joule dissipation in the auroral ionosphere, *Geophys. Res. Lett.*, *87*(A7), 5184–5196, doi:10.1029/JA087iA07p05184.

F. Honary, A. J. Kavanagh, A. Senior, and P. Wild, Department of Physics, Lancaster University, Lancaster LA1 4YB, UK. (p.wild1@lancaster.ac.uk)